J. Fluid Mech. (1996), *vol.* 310, *pp.* 61–87

Convection in a long box driven by heating and cooling on the horizontal boundaries

By J. J. STURMAN, G. N. IVEY AND J. R. TAYLOR†
Department of Environmental Engineering and Centre for Water Research,
The University of Western Australia, Nedlands, Western Australia, 6907, Australia

(Received 7 September 1993 and in revised form 15 September 1995)

Convection driven by spatially variable heat transfer across the water surface is an important transport mechanism in many geophysical applications. This flow is modelled in a rectangular tank with an aspect ratio, H/L, of 0.1 (where H and L are the tank height and length, respectively). Heat fluxes are applied through horizontal copper plates of length 0.1 L located at the top of one end of the tank and at the bottom of the other end. Experimental flows have been forced with heating at the bottom of the tank and cooling at the top, which gives rise to unstable convection in the end regions. Using water and a glycerol/water mix as the experimental fluids, flow visualization studies and measurements of temperature, velocity and heat flux have been made. Flow visualization studies revealed that complex unsteady turbulent flows occupied the end regions, while cubic velocity profiles characterized the horizontal laminar flow in the interior of the tank. Simple scaling arguments were developed for steady-state velocity and temperature fields, which are in good agreement with the experimental data. In the current experiments the portion of the plates closest to the tank interior (and to the tank endwall in the case of the glycerol/water experiments) were occupied by laminar boundary layers, while the remainder of the plates were occupied by turbulent flow. An effective Rayleigh number Ra^* was defined, based upon the portion of the plate occupied by turbulent flow, as was a corresponding modified Nusselt number Nu^*. The heat transfer was well predicted by classical Rayleigh–Bénard scaling with the Nusselt number $Nu^* \sim Ra^{*1/3}$. The range of Ra^* was $4.3 \times 10^5 \leqslant Ra^* \leqslant 1.7 \times 10^8$. Scaling arguments predicted the triple occupancy of the plates by differing boundary layer regimes within the range of $10^5 \leqslant Ra^* \leqslant 10^{14}$.

1. Introduction

Convection driven by spatially variable heat transfer across the water surface is an important forcing mechanism in driving horizontal exchange flows in many geophysical applications, such as lakes and reservoirs, monsoon dynamics, polar oceans, sea breeze flows and coastal ocean dynamics. In the side arms of reservoirs and lakes, for example, sheltering from the wind and sun can give rise to regions of latent, sensible and radiant heat flux which differ greatly from those in the main body of water. Although the causes of the differential heat fluxes vary from situation to situation, the consequences are the same: the creation of horizontal temperature and hence density gradients in the near-surface regions which, in turn, drive horizontal flows.

In lakes and reservoirs, such flows transport not only heat but also passive tracers such as chemical and biological species, and parameterizing these horizontal transports

† Present address: Australian Defense Force Academy, Northcott Drive, Campbell, ACT 2601, Australia.

is central to modelling and managing water quality in natural water supply systems. In the side arms of reservoirs and lakes, sheltering effects are common and lead to regions of the water surface with little or no wind stress acting on them, whereas other parts are fully exposed to the wind stress. This has two effects. First, it promotes rapid deepening of the mixed layer in the exposed regions driven by the momentum input of the wind (e.g. Maxworthy & Monismith 1988). Secondly, the net heat flux due to the combination of radiant, sensible and latent heat fluxes will vary greatly in the horizontal direction as the sensible and latent flux terms are almost linearly dependent on the local wind speed. Depending on the sign of the heat flux, this can either assist or counteract the effect of the deepening of the surface mixing layer due to the stirring from the wind stress. Our focus in this work is on the forcing due to the differential heat fluxes alone.

In temperate latitudes, the maximum radiant flux can be up to approximately 1000 W m^{-2}, while sensible and latent heat fluxes can be as high as 700–800 W m^{-2}, depending on wind speed (Imberger & Patterson 1990). Coates & Patterson (1993) suggest that the lateral fluid flow and heat flux due to the incident radiant flux alone is independent of the depth of penetration of the radiation and drives laminar flows. On the other hand, if the latent and sensible heat fluxes are negative (i.e. out of the water surface), this creates a region of convective instability and it is not clear whether the observations for laminar flows can be applied to these transitional and turbulent flows. It is clear that a horizontally variable heat flux source at the surface will give rise to flows which are significant in controlling the lateral exchange processes in lakes and reservoirs, as observed in field measurements by Monismith, Imberger & Morison (1990), for example.

Continental shelves provide the setting, in some circumstances, for dense water to convect from the surface through the entire depth of the water column, and then to proceed along the sloping bottom to provide an exchange flow with the ocean. In the Antarctic such a situation occurs in the Weddell and Ross Seas, where rejection of salt by ice formation provides the dense fluid (Killworth 1983). In temperate latitudes substantial surface heat fluxes out of the water can be induced in winter by both sensible heat flow and by evaporative cooling promoted by strong winds, inducing a similar process of dense (cold) water convecting to the bottom and providing a mixed layer over the depth of the shelf, as observed in the Adriatic Sea for example (Malanotte-Rizzoli 1991).

In the polar oceans, understanding the dynamics of these convectively driven flows is central to understanding the circulation and horizontal heat transport in the surface layers. While ice leads in the pack-ice represent only a small fraction of the surface area, they are responsible for a large fraction of the total heat flux. Badgley (1966) estimates they are responsible for a heat flux from the Arctic Ocean equal to the flux through the rest of the pack ice cover, even though the leads occupy only 10% of the surface area. Large negative heat fluxes drive vigorous vertical turbulent convection beneath the surface of the lead. While the descending thermals penetrate to the seasonal pycnocline, they are not energetic enough to penetrate this barrier and consequently drive horizontal flows above the pycnocline (Noh, Fernando & Ching 1992) with a compensating return flow at shallower depths with magnitudes as high as 5 cm s^{-1} (Morison *et al.* 1992).

In order to study frontogenesis and sea breeze dynamics (see Mitsumoto, Ueda & Ozoe 1983), the effect of turbulent stirring on horizontal buoyancy-driven flows has been investigated in the laboratory experiments of Linden & Simpson (1986), with uniform stirring induced by bubbling from below. Lemckert & Imberger (1993) studied

intrusive flows generated by turbulent bubble plumes at one location and found that the turbulence internal to the intrusions did not influence the spreading characteristics. It remains unclear, therefore, whether Morison *et al.*'s (1992) contention that the adjustment flows may be either laminar or turbulent, depending upon the strength of external forcing, is valid. Furthermore, for how long is the internal turbulence sustained, and does it affect the horizontal exchange flows?

Much work has been done on cavity convection flows with low aspect ratio with the forcing established by vertical hot and cold endwalls (e.g. Cormack, Leal & Imberger 1974; Bejan 1984). However, the current arrangement is more relevant to modelling geophysical flows, owing to the configuration of the forcing, and the fact that the interior flows are driven by unstable turbulent boundary layer flows over the plates.

Flows driven by spatially variable heat flux across the water surface, whether in lakes or the oceans, have a number of features in common: differential vertical heat transfer through horizontal surfaces creates horizontal density differences; the resulting horizontal adjustment flows are characterized by low aspect ratio in terms of depth to length; the flows are turbulent in the source regions and possibly in the interior; and the flows are likely to be unsteady as the forcing is time dependent. While important, field observations of these horizontal exchange flows are both difficult and costly to make. Accordingly, we have conducted a laboratory experiment in a novel configuration described below, which is designed to model more closely such flows. Preliminary results were described in Sturman, Ivey & Taylor (1992). The purpose of this paper is to describe the flow and heat transfer in a tank driven by a lateral gradient of temperature, applied in such a manner that the flow at each end is convectively unstable.

2. Experimental apparatus and methods

The experiments were conducted in a tank (see figure 1) 1000 mm long, 100 mm high and 300 mm wide, constructed of 15.2 mm Perspex sheet and insulated with 85 mm polystyrene foam on the bottom surface and 25 mm foam on all other surfaces. The principal experimental fluid was water, consistent with our interest in geophysical flows. In order to extend the range of Rayleigh numbers for which experiments were conducted, we ran a limited number of experiments using a glycerol/water mix of 77.9 % glycerol by weight. Copper cooling and heating plates 100 mm long are shown at the upper left and the lower right horizontal surfaces respectively. Axes are defined in figure 1. Chilled water and heated water were pumped from reservoirs through the manifolds backing the cold and the hot plates respectively. The hot water reservoir temperature was controlled with a Julabo electronic temperature controller maintaining the hot plate temperature to better than 0.1 °C. The chilled water reservoir temperature was cooled to below the desired temperature by a refrigeration unit. The cycling of the compressor caused severe oscillation of the temperature (up to 2.5 °C) and accurate water temperature was obtained by heating the cold water with a Julabo electronic temperature controller set to the desired temperature, with a resultant cold manifold water temperature accurate to better than 0.1 °C after starting transients passed.

Each plate temperature was monitored with two thermistors attached on the manifold sides of the plate and located about 25 mm from the sidewalls of the tank. Inlet water temperatures to the manifolds were also measured. Temperatures within the tank were measured by thermistor traverses from tank top to bottom of one second duration, at the sampling rate of 50 Hz. Access ports in the top of the tank allowed

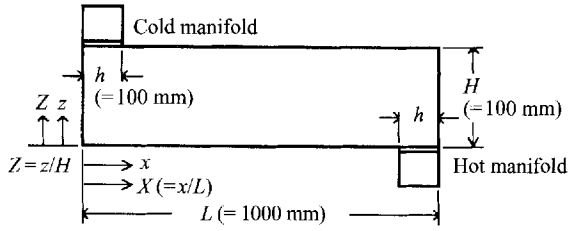

FIGURE 1. Schematic diagram of the tank, with definition of axes.

traverses (z-direction) to be made at locations spanning most of the length of the tank (x-direction) except for the range $0 \leqslant x \leqslant 100$ mm, where the chilled water manifold prevented the location of access ports. All thermistor temperature measurements were accurate to 0.01 °C, having been calibrated against a platinum resistance thermometer.

Velocity measurements within the tank were made by seeding the tank with Pliolite particles of less than 75 μm diameter. The tank was illuminated in the $Y = 0.47$ plane with a (vertical) sheet of laser light about 10 mm thick. ($Y = y/W$, where y is into the page in figure 1 and the width $W = 300$ mm.) Particle motion in the laser illuminated sheet was recorded onto video tape through windows in the insulation by means of a CCD camera, located to the side of the tank with the camera axis parallel to the y-direction. Image pairs were subsequently digitized for processing using a particle image velocimetry (PIV) method developed by Stevens & Coates (1994). Sub-pixel interpolation was subsequently employed in the manner of Willert & Gharib (1991). Typical time intervals between the pairs was 7/25 to 1 s, and the accuracy of the velocity measurements was 0.05 mm s^{-1}. This was determined by allowing the tank to become 'quiescent' overnight and by measuring the 'quiescent' velocities, which typically were less than 0.05 mm s^{-1}. This is a conservative estimate of the errors of the magnitudes of the velocities. Willert & Gharib (1991) claim a greater accuracy than this for the PIV process.

Heat flow from hot to cold plate is expressed as a Nusselt number (Nu), defined as the ratio of the total heat flow from plate to plate to the conduction heat flow from plate to plate with no fluid motion. Measurements of the convective heat flux were made across the centre-plane $X = 0.5$ by integrating the product uT from $Z = 0$ to $Z = 1$, where u is the local x-component of velocity and T is the local temperature. Adjustments were then made to this convective heat flux to allow for streamwise conduction, and for conduction and steady convection in the vertical direction. The Appendix gives a more detailed account of how Nu was calculated.

Heat losses from the tank were found by measuring the time taken for stirred hot water in the tank to fall by an easily measurable temperature (about 0.3 °C). Several runs were made and an overall (conduction and convection) mean heat transfer coefficient was calculated for the tank. Actual heat losses (or gains) were then calculated from experimental temperature profiles within the tank for each run. The laboratory air temperature was essentially at the mean tank temperature. The important quantity to evaluate was the degradation of the heat flow between the hot and the cold plates and thus the absolute values of heat gains and losses to and from the tank were added to give a total error for degradation of the plate to plate heat flow. The error was around 1 % for water at low Ra and less as Ra increased, where Rayleigh number is defined in this paper as $Ra = g\alpha h^3 2\Delta T/\nu\kappa$, where $2\Delta T$ is the total temperature difference between the plates and h the length of the plate in the x-direction. For the glycerol/water mix the tank heat loss error was estimated to be

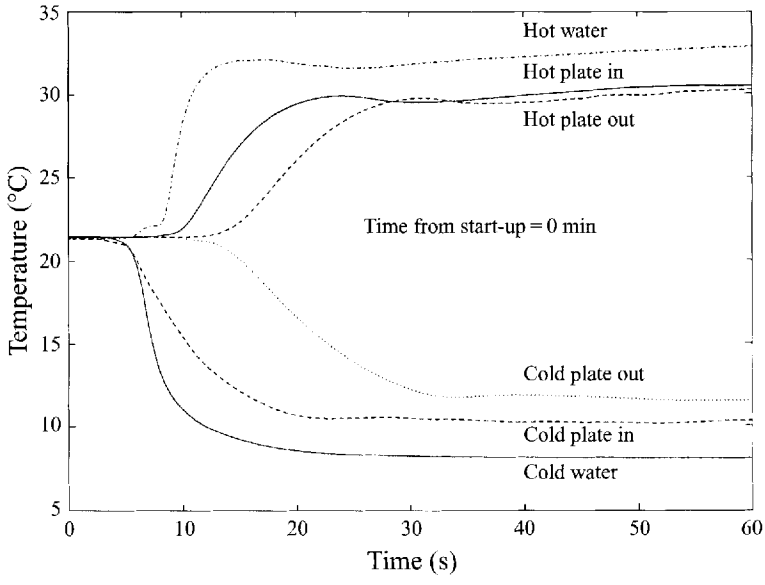

FIGURE 2. Plate transient temperatures.

about 4%. As will be seen later, the maximum temperature difference between the horizontal hot and cold streams in the tank interior was about 1 °C regardless of *Ra*. At the lowest and the highest *Ra* the temperature differences between plates were approximately 7 °C and 22 °C, respectively. Mixing of incoming cold flow over the hot end region lowered the fluid temperature to almost room temperature (and vice versa at the cold plate end of the tank) implying this experiment had intrinsically low heat flux degradation, as the above calculations indicated. In the experimental apparatus used here, we were able to attain Rayleigh numbers in the range $2 \times 10^7 \leqslant Ra \leqslant 3.3 \times 10^8$ and, as will be seen, the more pertinent Ra^* ranged over $4.3 \times 10^5 \leqslant Ra^* \leqslant 1.7 \times 10^8$.

Prior to the start of an experiment, water (or glycerol/water) in the tank was allowed to become quiescent overnight. Each manifold was filled with water at the tank bulk temperature, which was also the laboratory temperature. Pre-heated and pre-chilled water was pumped at start-up to the hot and cold manifolds, respectively. This provided a pseudo-step-function temperature increase (or decrease) at each plate. Figure 2 is an example of the measured heated and chilled water temperatures, and the temperature responses of the plates. There is a slight time difference between the entrance of hot and cold water in the manifolds of at most 5 s, and a similar difference in the responses of the plate temperatures. After 20 s the major component of the transient response of the plate has passed. Start-up of the plate temperature differences is difficult to locate precisely in time, because of the time taken to flush room temperature water from the manifold. In this paper we take it to be 15 s on the abscissa of figure 2. Notice that the temperatures measured on the opposite ends of the hot plate are closer to each other than the corresponding measurements on the cold plate. This was due to the cold water inlet port being relatively closer to the thermistor at the 'cold plate in' position than was the hot water inlet port in relation to the thermistor at the 'hot plate in' position. Short-term temperature fluctuations of the copper plates were less than 0.1 °C and long-term temperature drift over several hours was the same after starting transients had passed. The filling time (t_f) is the time taken for the whole of

the fluid in the tank to pass once through both 'boundary layers' on the plates and is given by $t_f \sim HL/(u\delta)$, where u is the horizontal boundary layer velocity scale and δ is the boundary layer thickness. (See §4 below for further development of the expression.) In order to give some physical meaning to time in the following discussion, approximate times will be quoted, referenced by the filling time (t/t_f): t_f is about 1.3×10^3 s for the glycerol/water experiments and ranged from 1.8×10^2 s for the high-Ra water experiments to 3.1×10^2 s for the low-Ra water experiments. The plate transients of $O(15$ s) are thus one order of magnitude below the time to thermal steady state for the cavity in the water case and two orders of magnitude below the time to steady state in the glycerol/water case. This gives us confidence that measurements in the steady-state region approach those expected from a step-function start. Measurements taken close to start-up (i.e. $t/t_f < O(1)$) reflect the actual start-up conditions of the experiments, rather than idealized step-function (or other) starting functions.

3. Description of the flow

3.1. *Detailed description*

The results to be discussed in this section are processed from video recordings of the water flow seeded with Pliolite particles and (separately) with rhodamine, which gave a better immediate view of the plumes rising from the heated plate when velocity fields were not required than did raw or integrated particle images. Records were taken in three regions of the tank: the heated end region near start-up time, a portion of the tank including the heated end region at large times, and at the centre of the tank (excluding end regions altogether) at times both near start-up and at large times. These records give good insight into both the gross features and smaller-scale events in the flow. Corresponding detailed flow visualization was not undertaken for the glycerol/water experiments. There the flow visualization was confined to the minimum necessary to process the data from the extended range of Rayleigh numbers.

The first records are those over the heated end region. Figure 3(*a–k*) is a sequence of images derived from a video tape record, the contents of which were integrated over 8 frames. Pliolite particles have been injected prior to start-up into the water above the hot plate using a syringe charged with a concentrated suspension of 5 g l^{-1}. Date and time data are imposed upon the visible edge of the upper wall of the tank and thermistor access ports can be seen in the same wall.

3.1.1. *Initial flow: the end region*

In figure 3(*a*) buoyant plumes can just be seen above the hot plate at approximately 6 s after start-up. An individual plume is clearly visible at the leading edge of the hot plate, with cold fluid penetrating across the leading edge a short distance and displacing the heated fluid. The progress of the buoyant plumes ascending from the plate is seen vividly in figure 3(*b*), with 'mushroom' structures having risen up to one third of the tank height by about 11 s after start-up. The nose of the cold fluid displacing the heated plumes has both advanced further along the plate and lifted slightly off the plate. Upstream of the leading edge are two coherent clouds of particles marked 'A' and 'B' with long arc-like structures convex to the lower left corner of the image. These can be identified with two less elongated clouds in figure 3(*a*) and, in turn, with more stretched clouds in figure 3(*c*). This suggests that at this stage the fluid displacing the original hot fluid is coming not from interior flows parallel to the horizontal walls of the tank, but rather from local recirculation in the end region. By

about 19 s after start-up ($t/t_f \approx 0.1$) in figure 3(*c*) an eddy has formed with the centre of circulation located at about $0.4H$ above the plate leading edge and just to its left. The vertical dimension of the substantially unmarked fluid penetrating above and along the hot plate is greater than it was in figure 3(*b*), the local intrusion having apparently strengthened and buoyant plumes penetrated about $0.6H$ above the plate.

By $t/t_f \approx 0.19$ in figure 3(*d*) (34 s after start-up) buoyant plumes have reached the upper wall, while mainly unmarked fluid has penetrated to about $0.6h$ along the plate and is squeezing the heated fluid towards the endwall. The nose of the unmarked fluid has lifted further and separation from the plate can be seen at about $0.2h$. The centre of circulation has shifted towards the endwall. Heated (though mixed) fluid in the upper portion of the tank has drifted somewhat to the left of the leading edge of the plate (bottom boundary), but it is not yet clearly established as an intrusion layer. In figure 3(*e*) (40 s after start-up, $t/t_f \approx 0.22$) the drift of heated fluid in the upper portion of the tank is starting to appear like an intrusion layer, especially with the frontal arc at the extreme upper left of the image. There is some evidence of three-dimensional flow, with lengthy streaks appearing in close proximity to apparently stationary particle clumps or clouds. The local intrusive flow over the hot plate has continued to squeeze the buoyant warm fluid towards the endwall and has penetrated vertically up to about $0.7H$. Separation of fluid from the hot plate is visible at about $0.2h$ from the leading edge.

In figure 3(*f*) (51 s after start-up, $t/t_f \approx 0.28$), the paucity of particles makes it difficult to interpret events near the plate. Small recirculating eddies are visible in the upper and (obscured partly by a screw) lower corners. The nose of the heated intrusion layer has passed out of the upper left field of view and more nearly approximates a parallel flow. It occupies roughly 0.3 of the height of the box. Neither the warm intrusion layer nor the cold intrusion from the other end have at this stage reached the far ends of the box. Until the hot and cold intrusion layers reach the opposite ends of the box from which they derive, fluid at the initial tank temperature is supplied to the end regions. The supply of cold fluid in figure 3(*f*) has ceased to be dominated by recirculation confined near the end region. Nevertheless, a general circulation still exists in the end region and some warm (though mixed) fluid appears to be recirculated into the oncoming cold stream. At the extreme upper left of the image is a very thin separated region extending to the left from above the 'C'. This apparently insignificant feature will be found to occur later at the same location as a significant separated region. In figure 3(*g*) (69 s after start-up, $t/t_f \approx 0.38$) the outgoing warm flow proceeds along the upper surface with a possible separation of the flow made difficult to interpret due to the presence of small bubbles. Three-dimensional flow could occur where the fluid moving down and to the left of the centre of circulation of the end region appears suddenly to stop as evidenced by the almost spot rather than streak appearance of particles.

Additional Pliolite particles have been introduced onto the floor of the tank upstream of the leading edge of the hot plate, but have not yet crossed the leading edge. Even so the separation point of the laminar boundary layer on the leading $0.2h$ of the plate is quite clear. The new particles are already across the leading edge of the plate in figure 3(*h*) (84 s after start-up, $t/t_f \approx 0.46$) in sufficient concentration to observe not only the point of separation, but two buoyant plumes which have been bent over by the incoming flow. Where there was strong circulation centred above the hot plate in figure 3(*g*), there is now a region of apparent quiescence (or possibly three-dimensional flow). The buoyant stream rising up the endwall turns and proceeds along the upper wall with a wave of wavelength about $0.6h$. A crest is marked 'D'. This contrasts with

(*a*)

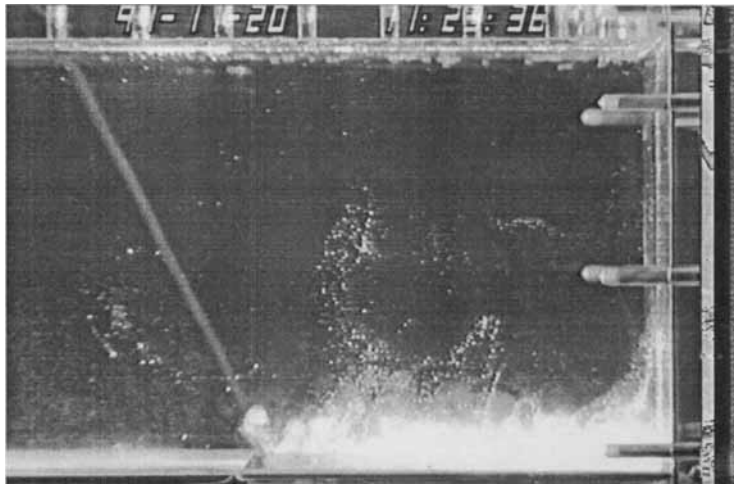

(*b*)

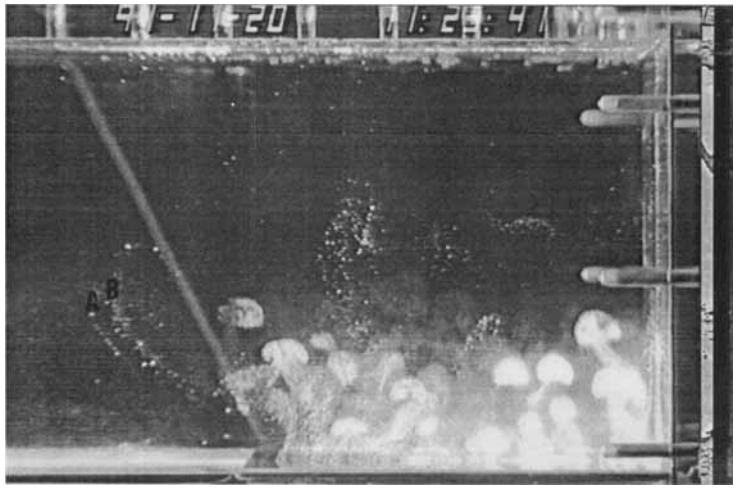

(*c*)

FIGURE 3. (*a–c*). For caption see page 71.

(*d*)

(*e*)

(*f*)

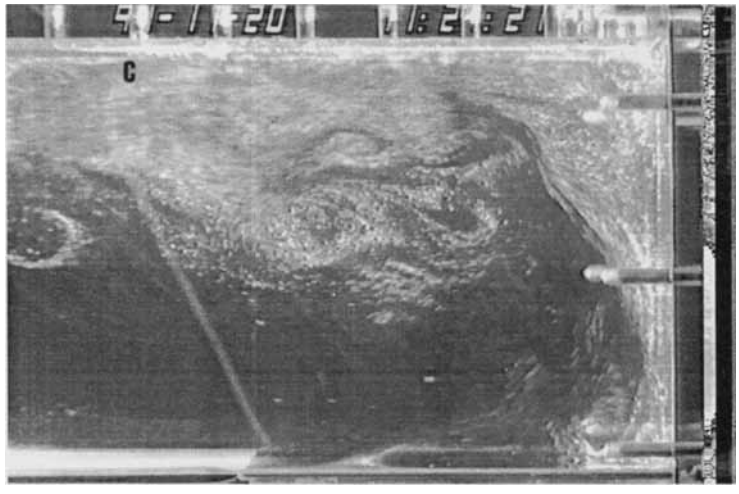

FIGURE 3. (*d–f*). For caption see page 71.

(*g*)

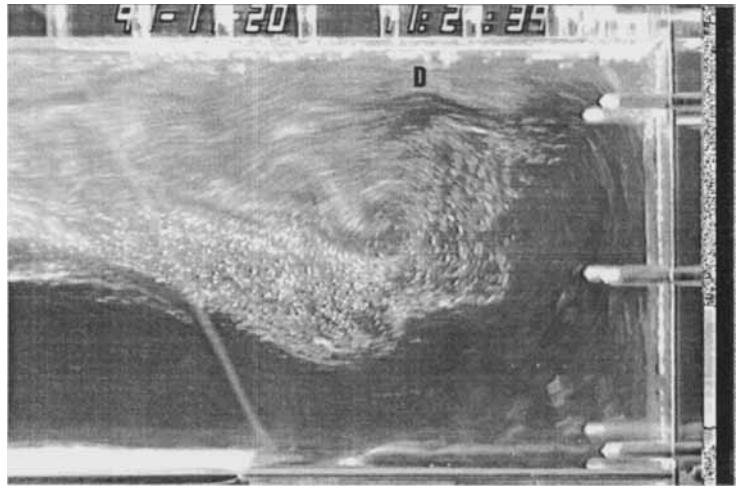

(*h*)

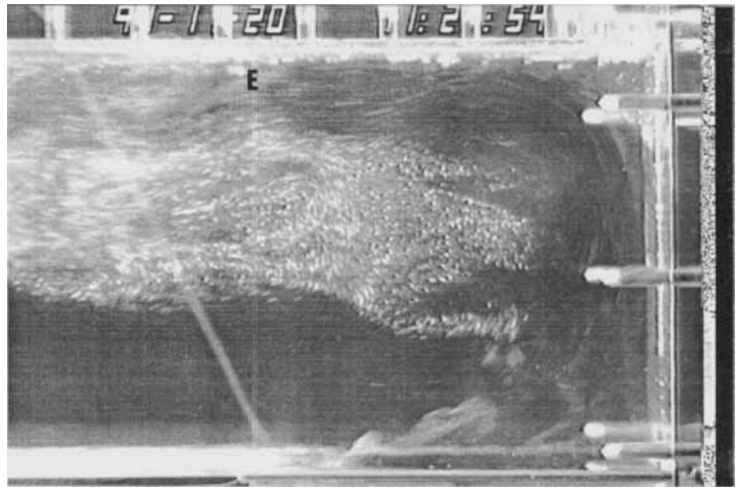

(*i*)

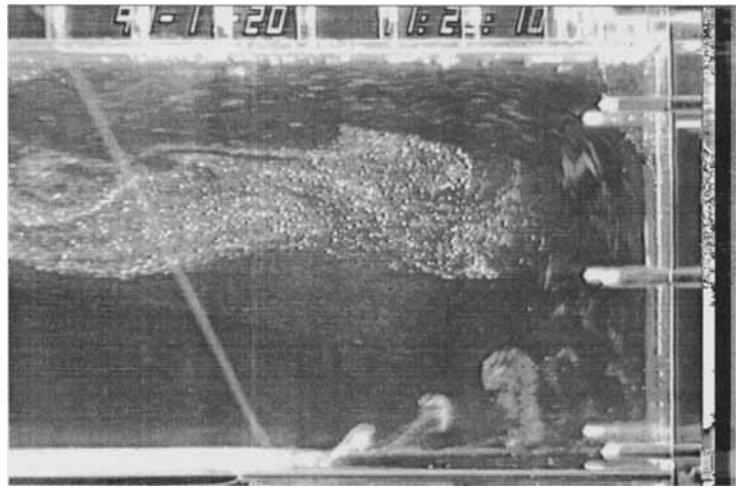

FIGURE 3. (*g–i*). For caption see facing page.

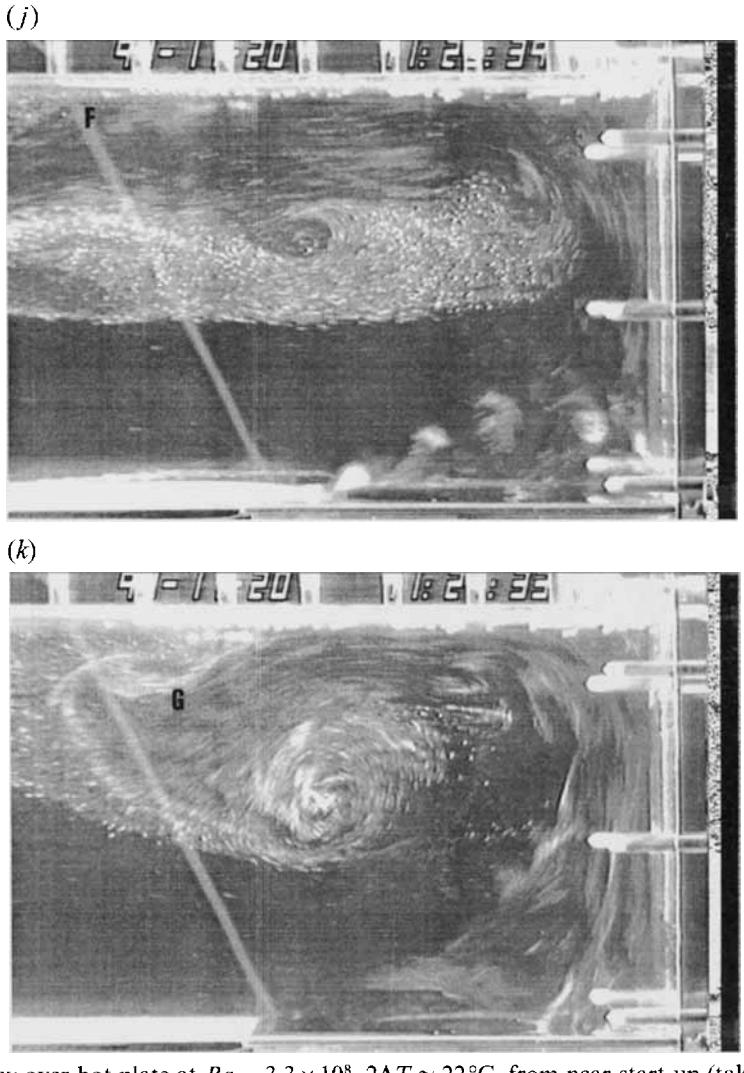

FIGURE 3. Flow over hot plate at $Ra = 3.3 \times 10^8$, $2\Delta T \approx 22\,^{\circ}\mathrm{C}$, from near start-up (taken as 15 s on figure 2), to 243 s after start-up ($t/t_f \approx 1.3$). The diagonal light line running from the upper left of the image to the leading edge of the hot plate is an out-of-focus stray thermistor lead outside the far wall of the tank and inside the insulation. Times after start-up are as follows: (*a*) 6 s, (*b*) 11 s, (*c*) 19 s, (*d*) 34 s, (*e*) 40 s, (*f*) 51 s, (*g*) 69 s, (*h*) 84 s, (*i*) 100 s, (*j*) 129 s, (*k*) 243 s.

figure 3(*h*) where there is also a wave but of wavelength about $0.3h$. A crest is marked 'E'. A region of separation at the extreme upper left is more obvious in figure 3(*i*) (100 s after start-up, $t/t_f \approx 0.55$); otherwise the warm intrusion flow on the upper wall is unremarkable. On the lower wall sufficient particles have now entered the plate region to reveal three clearly distinct buoyant plumes laid on their side by the mean flow, together with a clear location of the separation point, which has moved (compare with figure 3*f*). This image corresponds with the arrival over the hot plate of the cold intrusion layer nose.

3.1.2. *Near 'steady' flow: the end region*

The thickness of the apparently quiescent region between the counterflowing intrusions is noteworthy. This region persists and is still visible in figure 3(*j*) (129 s

after start-up, $t/t_f \approx 0.71$), though now some circulating structures are evident together with an apparently quiescent region at mid depth in the end region. Over the hot plate itself four plumes distorted by the vertically sheared horizontal flow are visible. Separation is still visible to the left of 'F' on the upper wall. A more dramatic example of separation from the upper wall is seen in the image in figure 3(*k*) (243 s after start-up, $t/t_f \approx 1.3$). A front is plainly visible in the upper left quadrant of the image, forming the 'top' of a diagonally inverted mushroom structure with two eddies trailing the front. The uppermost eddy forms the separated region on the top wall of the tank above 'G', while the eddy diagonally to the right forms a recirculating region above the hot plate near the tank centre in the z-direction. To the left of the front the magnitude of particle velocities is clearly lower than those behind the front. In the video record from which this image was derived, an internal wave was seen to build up and slow the intrusion flow in the upper left quadrant of the figure. The high-speed buoyant stream formed from coalescing plumes, and mixed on the way up the endwall, turned at the corner and fought against the slowing intrusion ahead of it, giving rise to the separated region on the top wall which subsequently retained its clear identity, though with varying strength and wandering location. The nature of the internal wave and its formation is not clear either from the images of figure 3 or from the video record from which figure 3 was derived. Particle densities above the hot plate are sufficiently low to make interpretation difficult in that region.

3.1.3. *Near 'steady' flow: the tank interior*

Consider now the region near the centre of the tank, but still at times close to t_f. The velocity field in figure 4(*a*) ($Ra = 2.0 \times 10^8$, $t/t_f \approx 0.9$) shows the passage of the lower (cold) intrusion layer, of thickness of about $0.3H$, past the centre of the tank. The nose of the intrusion is somewhat thicker than the tail and continuity requires that there is substantial displacement of fluid in the remainder of the tank. This is very evident immediately ahead of the nose of the intrusion layer. There is a substantial time difference between the passages across the vertical centreline of the tank of the two intrusion layers, the upper (hot) intrusion having already left the field of view of the video frames from which figure 4 was derived. The explanation for this was the discovery of a kink in the cold water supply line in the run from which this image was drawn, which meant that the start at the cold end was delayed by about 20 s compared with the heated end, that is by about $0.1t_f$. This is sufficient time for the upper intrusion to have left the field of view. Even so, on other images similar to that from which figure 4(*a*) was derived, but originating from a run where transient time profiles at each end were similar to those in figure 2, there appeared a time difference between the passage of the two intrusions across the centreline of the tank which was greater than the time difference between start-up at the two ends. This could be due to variations in thermal properties near the plates resulting in stronger plume formation at the hot end (lower viscosity or higher α providing the hot intrusion with a higher buoyancy flux), but without further evidence the reason for this effect is uncertain and warrants future investigation. At $t/t_f \approx 2.3$ the whole depth of the tank is occupied by horizontal counterflow. The velocity field (figure 4*b*) shows that the line of zero velocity slopes down to the right, while other records show a less or non-sloping zero-velocity line, suggesting the existence of cavity-scale oscillations, at least at these relatively early times. This effect was observed in other runs, even for long times ($t/t_f > O(1)$).

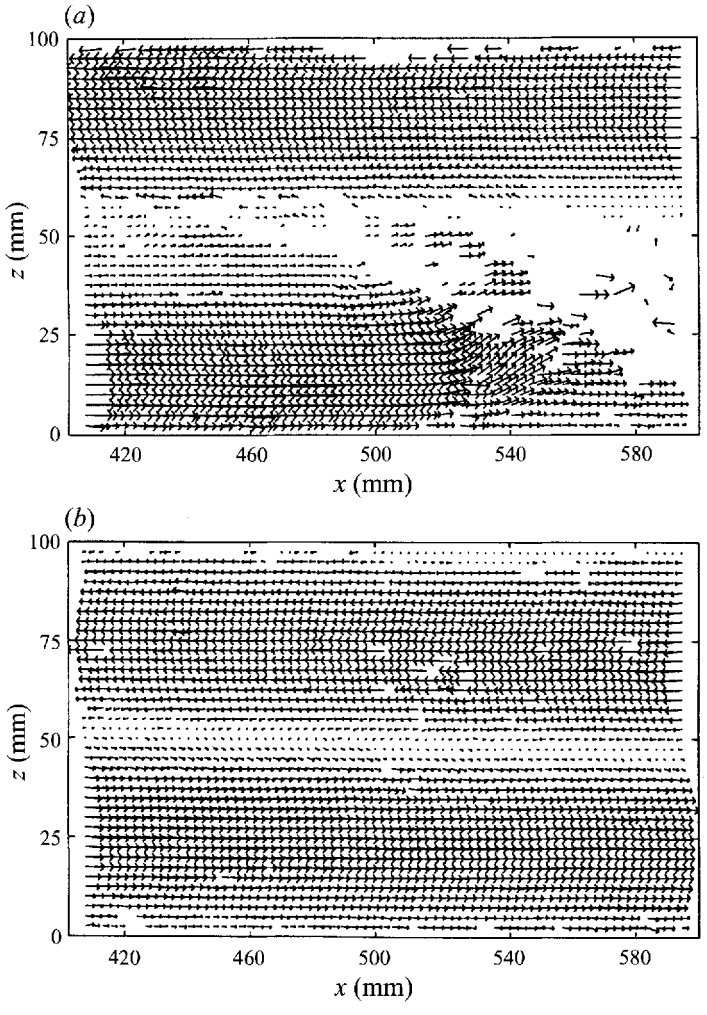

FIGURE 4. Velocity field at the tank centre, $Ra = 1.98 \times 10^8$: (*a*) $t/t_f \approx 0.9$ and (*b*) $t/t_f \approx 2.3$. The scale of velocity vectors is approximately 21 mm s^{-1} per smallest scale division on the x-axis.

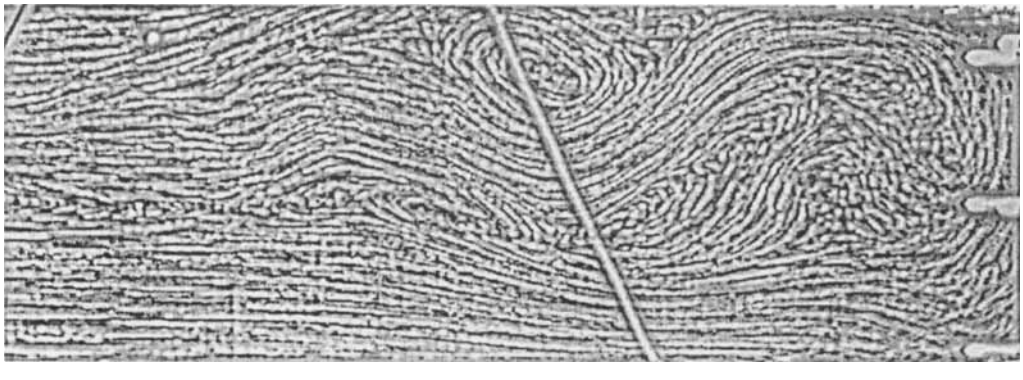

FIGURE 5. Streak image at $Ra = 3.22 \times 10^8$, $t/t_f \approx 1 \times 10^2$ at the heated end of the tank.

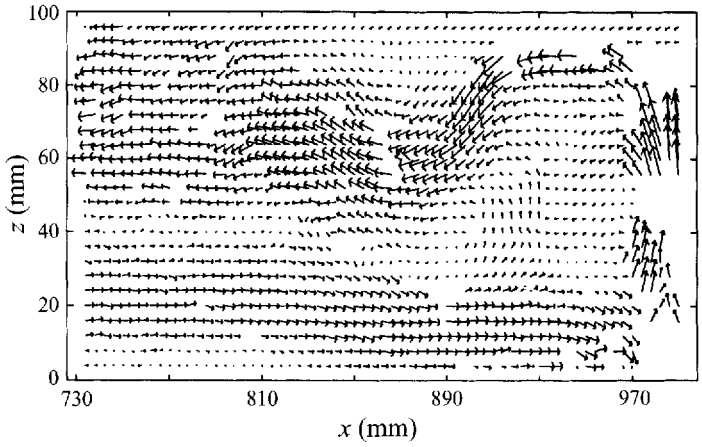

FIGURE 6. Velocity field corresponding with figure 5. The scale of velocity vectors is 23 mm s^{-1} per smallest scale division on the x-axis.

3.1.4. *'Steady' flow: the end region*

Consider now the (heated) end region at long times. Video frames were integrated over about 7 s to produce streak images. Velocity maps generated from PIV were produced from a time interval of 7/25 s, within the 7 s span of the integrated images. Figure 5 shows the streak image at $Ra = 3.22 \times 10^8$ and at $t/t_f \approx 10^2$ and the corresponding vector field is shown in figure 6. The overall impression of figure 5 is very similar to that obtained from figure 3(k). The process of integrating the images has removed the detail from immediately above the plate. On the endwalls the 'thickness' of the buoyant stream is approximately $h/4$. The stream turns at the top right-hand corner and moves left along the wall, while below in the interior of the tank lies a semi-quiescent region. At about $X = 0.9$ (the leading edge of the plate) the stream detaches from the top wall and plunges into the interior of the tank to return to the top wall at around $X = 0.8$, where it is of thickness $H/2$. Velocities adjacent to the endwall and in the plunging stream are large compared with the counterflows at the centre of the tank (up to 3 times the magnitude). Figures 5 and 6 do not represent a steady-state picture of the flow in the end regions. The flow is actually quite unsteady, as seen in the video records from which the figures were derived. For example the separated region on the upper wall expands and shrinks and moves laterally along the wall as much as $\Delta X = 0.05$. The heated stream separating from the upper wall plunges into the interior of the tank by amounts varying by as much as $\Delta Z = 0.3$. At the maximum extent of downward penetration some warm fluid appears to feed back into the cold stream approaching the hot plate. The semi-quiescent region centred above the hot plate likewise distorts and changes in size. The eddy whose existence is but hinted at in figure 5 at about $X = 0.8$ and $Z = 0.4$ grows to a significant entity and subsequently decays. The time scales of the unsteadiness of these major features are of the same order of magnitude as t_f and are not simply periodic.

To show the detail above the hot plate, rhodamine was introduced into the fluid both upstream of the plate and on it (see figure 7). The boundary layer was laminar for a short distance from the edge of the plate and separation took place at a similar location to that seen in figure 3(i). Buoyant plumes rose from the plate in figure 7 and were swept along toward the endwall by the mean flow. This is very similar to what was seen earlier in figures 3(i) and 3(j). The maintenance of coherence in the plume structures

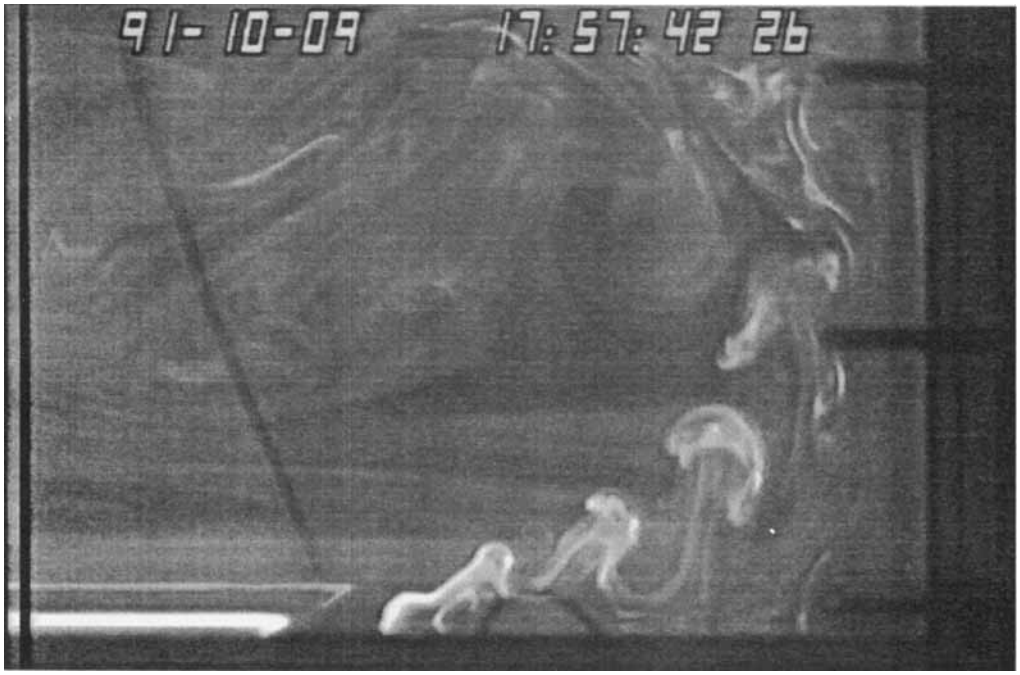

FIGURE 7. Laser illuminated rhodamine image, $Ra \approx 3.3 \times 10^8$, $t/t_f \sim O(10^2)$.

for greater than half the height of the endwall is remarkable. In some video records the buoyant plumes were not as evident, especially at lower Rayleigh numbers, but similar general behaviour was apparent.

3.1.5. *'Steady' flow: the glycerol/water case*

Figure 8 shows a velocity vector map above the hot plate (located from 900 to 1000 mm) when the experimental fluid is glycerol/water. As well as general similarities, there are strong contrasts between this image and the corresponding figures 6 and 7 for water. The presence of a buoyant plume (or plumes) occupying a portion of the plate is still evident, together with a strong flow turned up the endwall. It is noticeable, though, that the 'turbulent' flow occupies much less of the plate than in the water case, with a significant difference being the extended region close to the endwall where the impact of buoyancy is suppressed. The separation feature on the upper wall, which was so evident in the water case, is missing in the glycerol/water image (a similar observation was made by Ivey 1984 in an experiment with heated and cooled vertical endwalls) and thus it seems reasonable to infer that the separation feature in the water images is an inertial feature.

3.2. *Summary description*

When the heating (and cooling) of the plate(s) is switched on there is a small time delay while heat diffuses into the water until the critical boundary layer thickness is reached, at which time buoyant plumes form and rise from the hot plate. These attempt to rise over the total height of the tank at the same time as a circulation of fluid in and near the end region develops and sweeps the rising buoyant plumes towards the endwall. The flow is turned 180° by the endwall, and an intrusion layer subsequently moves out along the upper wall, initially with a thickness of about 30% of the tank height. A

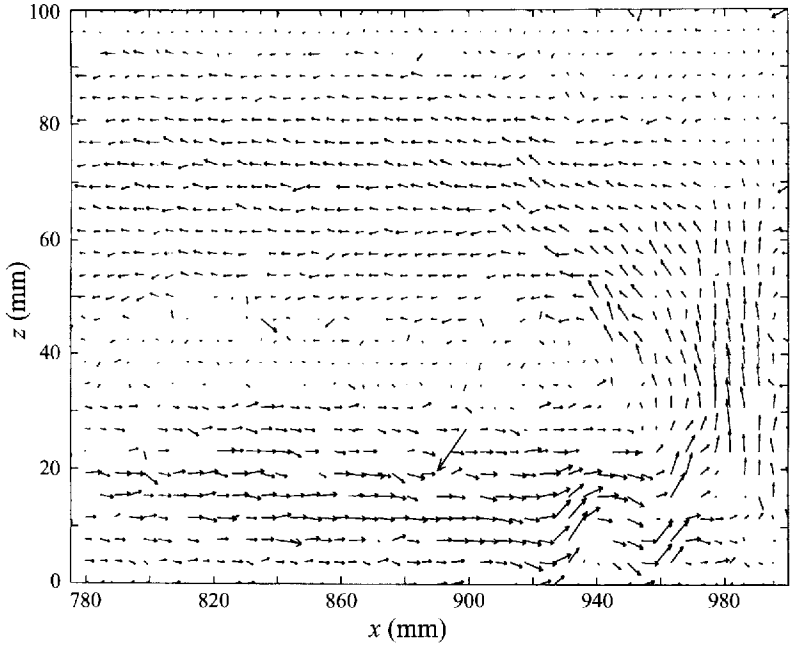

FIGURE 8. Velocity vector map for the glycerol/water experiment, $Ra = 2.04 \times 10^7$, $Ra^* = 4.27 \times 10^5$, $t/t_f \approx 4.1$. The scale of the velocity vectors is 2.8 mm s^{-1} per smallest scale division on the x-axis.

region of local circulation remains in the end regions at times of the order of t_f and greater. At a time of about t_f as estimated in §4, fluid is supplied over the hot plate by the cold intrusion layer. The first 20% of the hot plate is occupied by a laminar (diffusive) boundary layer, after which buoyant plumes are usually seen to rise and to be swept towards the endwall by the mean flow. The nature of the 'boundary layer' on the downstream 80% of the plate appears to be transitional between laminar and fully turbulent. A substantial region of separation occurs on the upper wall about $0.8 \leqslant X \leqslant 0.9$, which results in the outgoing intrusion layer occupying half the height of the tank. While there is at least a superficial similarity between the separation feature and what is seen in cavities with heated and cooled endwalls (e.g. Patterson & Armfield 1990), it is clear that overall the end regions bear little resemblance to what is seen in cavities with heated and cooled vertical endwalls. The above summary cannot be applied in detail to the flow seen when the working fluid is the glycerol/water mix. The separation feature is missing and the extent of the plate where the flow is effectively turbulent is truncated by a significant viscous region adjacent to the endwall.

4. Scaling

The purpose of this section is to develop some simple scaling arguments to describe the flow, which will enable interpretation of the steady-state experimental results. From the flow visualization results of the previous section it is clear that the dominant flux of heat from the hot plate is not merely via the medium of a laminar boundary layer and yet, because of the strong coherence of the buoyant plumes well up the height of the box, it appears unlikely to be due to fully turbulent flow over the entire plate.

Consider first the simplifying case where the vertical heat flux is controlled by turbulent processes over the whole plate. The existence of a laminar boundary layer of

length h_c near the leading edge and the occurrence of a viscous region of length h_t close to the endwall when the fluid is glycerol/water, will be accounted for later.

With these assumptions, above the heated plate (or below the cooled plate) the dominant balance in the energy equation at steady state is between horizontal convection and vertical turbulent transport of heat:

$$u\frac{\partial T}{\partial x} \sim \frac{\partial \overline{(w'T')}}{\partial z}, \tag{1}$$

where u and w are horizontal and vertical velocity components, T is temperature and primed quantities are fluctuations about the temporal mean value. The temperature difference from the surface to fluid in the boundary layer can be expressed in terms of surface buoyancy flux and height above the surface as (e.g. Chou, Atlas & Yeh 1986)

$$\Delta T \sim B_0^{2/3}/\alpha g z^{1/3}, \tag{2}$$

where B_0 is the buoyancy flux at the plate surface, α is the coefficient of thermal expansion of water, and ΔT is half the temperature difference between the heated and cooled plates. Chou *et al.*'s results derive from experiments in the planetary boundary layer, but Adrian, Ferreira & Boberg (1986) show that there is very good agreement between measured turbulent properties in laboratory experiments and in the atmospheric boundary layer. As the buoyancy flux within the freely convecting zone is directly proportional to the surface buoyancy flux (e.g. Chou *et al.* 1986, equation (5))

$$\overline{(w'T')} \sim B_0/\alpha g. \tag{3}$$

Substituting (3) and (2) into (1) with $x \sim h$ (the plate length) and $z \sim \delta$ (the unknown vertical boundary layer scale) we find that

$$u \sim B_0^{1/3} h/\delta^{2/3}. \tag{4}$$

Assuming that the turbulent stresses dominate over the inertial terms (cf. Patterson & Imberger 1980) then at steady state the horizontal momentum equation reduces to

$$0 \sim -\frac{1}{\rho}\frac{\partial p}{\partial x} - \frac{\partial}{\partial z}(\overline{u'w'}). \tag{5}$$

The corresponding vertical momentum equation is given by

$$0 \sim -\frac{1}{\rho}\frac{\partial p}{\partial z} + g\alpha T. \tag{6}$$

Eliminating pressure terms between (5) and (6), and assuming $\overline{u'w'} \sim w_*^2 \sim (B_0\,\delta)^{2/3}$, where w_* is the convective velocity scale, implies $\delta \sim h$ (recall h is the length of the plate), which is consistent with what is seen in figure 7. Thus from (4)

$$u \sim (B_0 h)^{1/3}, \tag{7}$$

which is essentially the same as the earlier suggestion by Phillips (1966).

Defining the time to steady state as the 'filling time' (that is, the time taken for the whole of the fluid in the tank to pass once through both boundary layers on the plates), then

$$t_f \sim HL/u\delta \sim HL/B_0^{1/3} h^{4/3}, \tag{8}$$

which, as seen in §3, compares favourably with the observed time scales.

From Turner (1973) the surface buoyancy flux (for water) can be expressed in terms of the temperature difference between the plate and the bulk tank fluid temperature as

$$\frac{\alpha F_H}{\rho C_p} = \frac{B_0}{g} = 2^{4/3} c \left(\frac{g\kappa^2}{\nu}\right)^{1/3} (\alpha \Delta T)^{4/3}, \tag{9}$$

where F_H is the heat flux at the plate surfaces, C_p is the specific heat, and κ and ν are the thermal and momentum diffusivities. Equation (9) is derived upon the assumption that the scaling

$$Nu = cRa^{1/3} \tag{10}$$

holds true, being the only possible scaling in which the heat transport is independent of the spacing between the horizontal plates. Though the length scale is eliminated in (10), it is important to note that the appropriate length scale for the Rayleigh number is the vertical spacing between the plates, which is the maximum extent of the penetration of the buoyant plumes. The results discussed in the review by Siggia (1994, p. 150) indicate that $c = 0.069$ is the appropriate value at $Ra = 10^7$, a representative value for the present experiments.

The observations described above indicate that the interior flow is essentially parallel. Consequently, we assume that the convective heat flux dominates over the diffusive flux in the x-direction. Thus there will be a non-zero vertical temperature gradient at the horizontal centreline of the tank if the horizontal convective heat flux is greater than the vertical diffusive heat flux, that is if

$$\rho C_p u \delta \Delta T_i > kL(\Delta T_i / H), \tag{11}$$

while ΔT_i is the deviation of the interior counterflow temperature from the mean tank temperature. Bearing in mind that $h = H$, $k = \kappa \rho C_p$ and taking u as given in (7), then (11) reduces to

$$B_0 > \kappa^3 / A^3 h^4, \tag{12}$$

where $A = H/L$.

Similarly, the condition for quiescent velocity at the horizontal centreline of the tank is that the horizontal momentum flux be greater than the vertical transport of momentum by viscous diffusion, i.e.

$$\rho(u\delta)\, u > \nu(\rho u / H) L, \tag{13}$$

or

$$B_0 > \nu^3 / A^3 h^4. \tag{14}$$

The Rayleigh number is defined in this paper as

$$Ra = gh^3 \alpha 2\Delta T / \nu\kappa, \tag{15a}$$

where $2\Delta T$ is the total temperature difference between the plates. Note that the (horizontal) plate length, h, is the appropriate length scale arising from the transport equations when we assume turbulent convection over the whole plate and this is also the scale of the maximum penetration upwards, δ, of the buoyant plumes. The definition (15a) is appropriate for very high Rayleigh numbers whose values will be made explicit later. As the present tank has $h = H$, at very high Rayleigh numbers $\delta \sim h$ still holds. If $H < h$ the scaling would need further modification. The definition (15a) needs to be modified for the more modest values of Rayleigh number of the current experiments. Define the effective length over which there is turbulent flow as $h_e = h - h_c - h_t$, where h_c is the distance from the leading edge of the plate at which the

laminar boundary layer becomes turbulent and h_l is the distance from the endwall of the tank at which the turbulent flow ceases (in the glycerol/water case in particular). Then an alternative Rayleigh number, Ra^*, may be defined as

$$Ra^* = gh_e^3 \alpha 2\Delta T/\nu\kappa. \tag{15b}$$

While (15*a*) is a convenient form of Ra to use in the laboratory situation, in the field a definition based upon heat flux rather than temperature difference is more suitable and, using equation (9), Ra may be written as

$$Ra = \{B_0 h^4/(c\nu\kappa^2)\}^{3/4}. \tag{16}$$

As can be seen in figures like figure 3(*i*), the boundary layer is laminar near the leading edge and an estimate can be obtained of the distance from the plate leading edge at which transition of this laminar boundary layer takes place, which will enable the evaluation of h_c for a range of Rayleigh numbers, though images like figure 3(*i*) are available only at one Rayleigh number.

The critical time for a growing laminar convective boundary layer to reach instability is given from the definition of thermal diffusion as

$$t_c \sim \delta_c^2/\kappa, \tag{17}$$

where δ_c, the critical thickness of the laminar boundary layer, is implied from the critical Rayleigh number (based upon ΔT) $Ra_c = 1108$. (At $Ra = 3.3 \times 10^8$ the order of magnitude estimate of t_c is $O(11)$ s which compares satisfactorily with plumes first being visible at 6 s after start-up in figure 3*a*.) The residence time of fluid in the laminar boundary layer is found using the estimate of the effective velocity u_e from the turbulent scaling of equations (7), (9) and (15*b*), with h replaced by h_e:

$$t_c \sim h_c/u_e \sim h_c h_e/\kappa Pr^{1/3} Ra^{*4/9}. \tag{18}$$

Equating t_c in (17) and (18) gives h_c in terms of Ra as

$$h_c/h^{2/3} h_e^{1/3} \sim Pr^{1/3} Ra^{-2/9}. \tag{19}$$

The coefficient of proportionality to convert (19) to an equality, C_c, can be found from images such as that in figure 3(*j*), resulting in $C_c = 15$ as the best estimate for water from our images. Note that this need not be of $O(1)$, as it includes constants and the critical Rayleigh number which have been excluded from (19) to avoid clutter.

Rossby (1969) suggests that transition to turbulence occurs at $Ra \approx 14000 Pr^{0.6}$ for $Pr \gg 1$, which leads to $Ra^* = 4.5 \times 10^4$ for water and $Ra^* = 4.7 \times 10^5$ for the glycerol/water mix ($Pr = 348$). An upper extreme for h_c is thus implied beyond which the scaling of (19) is invalid. At the other extreme, when 99% of the plate is occupied by 'turbulent' convection, $Ra^* \approx Ra \approx 10^{14}$ for water.

There is clearly a region on the plate close to the endwall where endwall effects change the balance of terms in the turbulent scaling, for the horizontal plate at least, for the glycerol water mix. Both experiments using glycerol/water were at essentially the same Rayleigh number, so that direct measurements of h_l from video images from one experiment were applicable to the other. This region was not observed for the water case, and this was consistent with the predictions of a simple model based on Heimenz flow (see Schlichting 1968) which predicted $h_l/h \approx 0.02$. As we are interested in modelling geophysical flows, we regard the existence of the laminar region of length h_l from the endwall as an inconvenient consequence of extending the range of Rayleigh numbers over which we tested our scaling to unrealistically low values for geophysical flows, but nevertheless to a region where the scaling was tested at its most adverse limit.

We have assumed in the scaling arguments that the dynamics of the tank are driven entirely by turbulent heat flow processes above the plate, and that the contribution to heat flow from molecular diffusive processes is negligibly small. A comparison of this neglected vertical diffusive heat flux with the vertical turbulent flux retained in (1) indicates that the assumption is valid provided $Ra > 1$.

The introduction of the modified Rayleigh number Ra^* in (15*b*) has prompted us also to define a modified Nusselt number Nu^* as the total convection heat flow from the portion of the plate occupied by turbulent convection, $\tilde{H}$, divided by the conduction heat flow from plate to plate were the fluid stationary and the plates of dimension h_e, using the conduction path length L^*_{cond} assuming the plates are of dimension h_e and are at the location where turbulent processes are occurring. Thus

$$Nu^* = \frac{\tilde{H} L^*_{cond}}{k h_e W 2\Delta T}. \tag{20}$$

Just as $Ra^* \to Ra$ as $Ra \to \infty$, so $Nu^* \to Nu$ as $Ra \to \infty$.

Velocity, temperature and heat flow results, mainly at steady state, will be presented in the next section, in the light of the simple scaling arguments developed above.

5. Velocity, temperature and heat flux results

Inequality (14) is satisfied by the present experimental arrangement with water at steady state, and so the counterflows should be less than half the tank height. Earlier it was noted that in figure 4(*a*) the initial intrusion layer (excluding the nose, which is a little thicker) occupies about 30% of the height of the tank. This is consistent with inequality (14) being satisfied. At times greater than the filling time the velocity profiles fill the tank in the vertical direction contrary to (14). The filling of the interior of the tank by the intrusion layers we hypothesize to be due to the separated transition on the upper wall in the region $0.8 \leqslant X \leqslant 0.9$, which appears as a more or less constant feature at some time soon after the filling time. In the glycerol/water case the two sides of the inequality (with h_e replacing h) are of the same order of magnitude and the test is inconclusive.

Separated regions with a similar appearance have been seen in boxes with heating and cooling on opposite (vertical) endwalls. The nature of the separated region in the latter case was tentatively suggested by Ivey (1984) to be an hydraulic jump. Subsequent numerical and experimental work by Patterson & Armfield (1990) and by Armfield & Patterson (1991) suggests that the feature is not an hydraulic jump in the conventional sense, and is caused by a combination of diffusion effects where the boundary condition changes from heated to non-heated walls, and by the pressure wave related to the arrival of the intrusion on the opposite wall of the box. These conditions do not apply to the conditions of the present experiments, as clearly there is not a sudden change of boundary condition at the upper right corner of the box and there is a vast difference between the boundary layer on the heated (vertical) endwall and the flow up the endwalls. No simple calculation could determine whether or not the separation feature could be characterized as an 'hydraulic' jump. The stream looks discrete in figures 5 and 6 upstream of the separation feature, and we have used the discrete stream method of calculation of Turner (1979, p. 65) taking velocity from figure 6, and temperature difference from figure 10 to find a Froude number of approximately 3. This leaves open the possibility that the flow is supercritical, and the nature of the separated region is the subject of future investigation.

Profiles of the horizontal velocity at the vertical centreline of the tank were found by averaging rows in vector maps across a span of about $0.125L$. Using equations (7), (9) and (18), and noting that by observation interior flow always occupies the full depth of the box (see figure 9*b*) at steady state, the horizontal velocity can be written in non-dimensional form as

$$U^* = \frac{uh_e}{\kappa(c\nu/\kappa)^{1/3}\,Ra^{*4/9}}\left(\frac{H}{2h_e}\right) = \frac{Pe}{2(cPr)^{1/3}\,Ra^{*4/9}}. \tag{21}$$

where the term $H/2h_e$ is included noting that each of the counterflows at $X = 0.5$ in the interior occupy the height $H/2$, whereas the discharge u_e from the turbulent boundary layer is over the scale $\delta \sim h_e$.

In order to evaluate (21) it is necessary to establish values of h_e. This is relatively straightforward in the case of water, where the determination of $h_e(= h-h_c)$ is directly available from (19). For the glycerol/water mix it is more difficult, given that now $h_e = h-h_c-h_l$. Furthermore, the boundaries of h_e and h_l were visually less clear in our video records than in the water case. After several trials this difficulty was resolved by plotting w^2 (w is the vertical velocity component) against position along the plate, resulting in a very sharp definition of the turbulent region and hence the determination of h_c, h_l and h_e.

Figure 9(*a*) shows U^* as a function of Z for six profiles taken at the centre of the tank at an intermediate Rayleigh number for water ($Ra = 1.98\times10^8$, $Ra^* = 9.36\times10^7$) and for very long times ($t/t_f \geqslant 10^2$ in every case). The profiles are separated in time from each other by $t/t_f > 10$. Figure 9 shows some variability in the velocity profiles at steady state. The variations in velocity are real; they are not measurement noise, which is about 0.005 in the non-dimensional scale of the figure. The scatter is consistent with the existence of tank-scale internal waves at long times as discussed earlier. The magnitude of the fluctuations is considerably greater near $Z = 0.25$ and $Z = 0.75$ than near the vertical centre, which is also consistent with this interpretation and clearly shows the presence of unsteady motion even at steady state.

Velocity profiles at the same location as those in figure 9(*a*) are shown in figure 9(*b*), for five different experiments for both water and the glycerol/water mix, plotted with the scaling of (21). The scatter is somewhat enlarged over that of figure 9(*a*), but not substantially so. The data for $Ra = 2.07\times10^7$ invite some comment. Two profiles of the five which constitute this experiment are noticeably outside the range of scatter of all the other data, especially near $Z = 0.2$ and to a lesser extent near $Z = 0.8$. There are two possible explanations for this. First, the run with the maximum deviation is close to start-up with $t/t_f \approx 1.5$, and this could account for the higher values. The run with the next highest deviation is at $t/t_f \approx 7$, the longest time for this experiment, which makes it unlikely to have elevated values due to start-up when points at intermediate times do not display the same elevation. Secondly, the combination of the seeding density and the quality of the video images for the two profiles led to their having a lower signal-to-noise ratio than for the other data. Note that the points (+) occur on the low side of the mean as well as on the high side. Other than this, the collapse of the data onto a line is strong support for the scaling. While the range of Rayleigh number is greater than an order of magnitude, it is important to note that the effective Rayleigh number Ra^* ranges from 4.27×10^5 to 1.69×10^8 for the data in figure 9(*b*). Furthermore, the lowest value of Ra^* is just below the value suggested by Rossby's (1969) criterion for transition to turbulence. Thus the scaling has held, even allowing the Rayleigh number to decline to the most adverse region for testing its validity. Note that the peak velocities suggest a constant of proportionality for the scaling

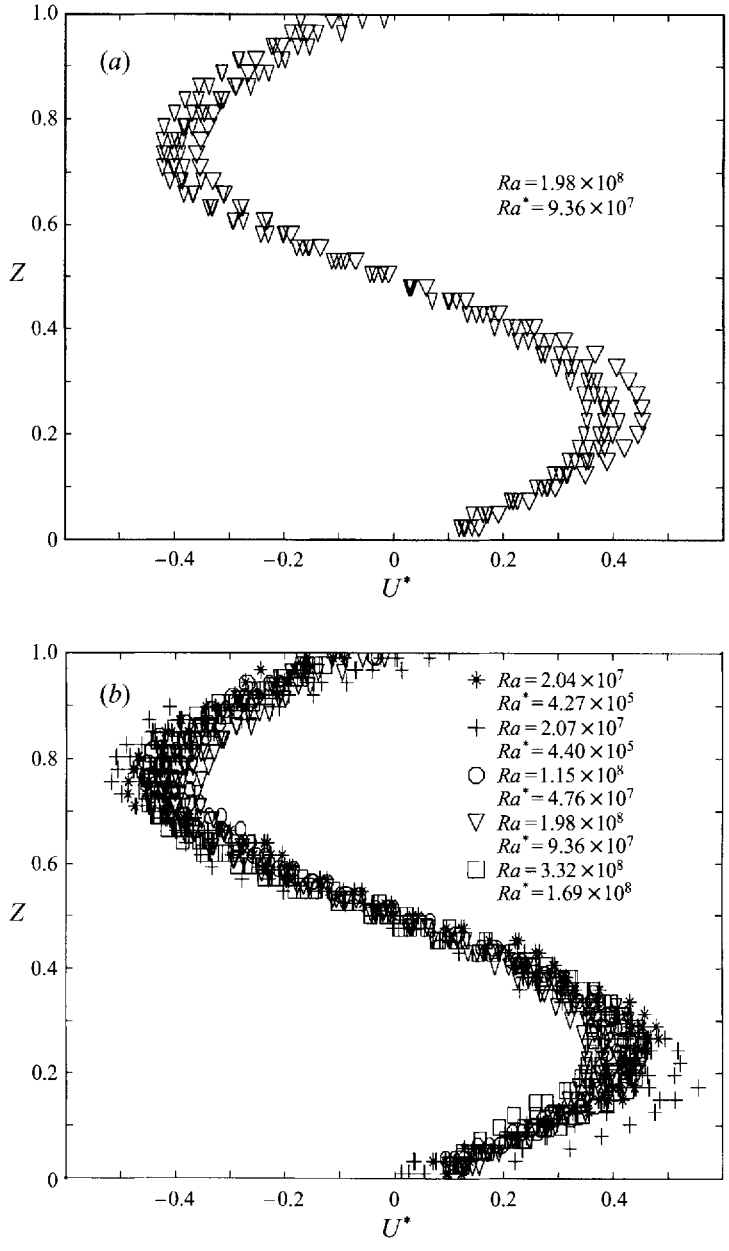

FIGURE 9. (*a*) Velocity profiles at $X = 0.5$, $t/t_f \sim O(10^2)$. Time between profiles $> 10t_f$. (*b*) Velocity profiles at $X = 0.5$; for water $t/t_f \sim O(10^2)$, time between profiles $> 10t_f$; for glycerol/water $1.5 \leqslant t/t_f \leqslant 8$, time between profiles $\approx t_f$. Note that the points (+) are on the low side of the mean as well as on the high side.

approaching 0.5. Overall, figures 9(*a*) and 9(*b*) are strong confirmation of the scaling in the previous section and the best fit description is

$$U^* = a_3 Z^3 + a_2 Z^2 + a_1 Z + a_0,$$

where

$$a_3 = 8.8636, \quad a_2 = -1.3363 \times 10^{-1}, \quad a_1 = 4.4999, \quad a_0 = -3.6667 \times 10^{-4}.$$

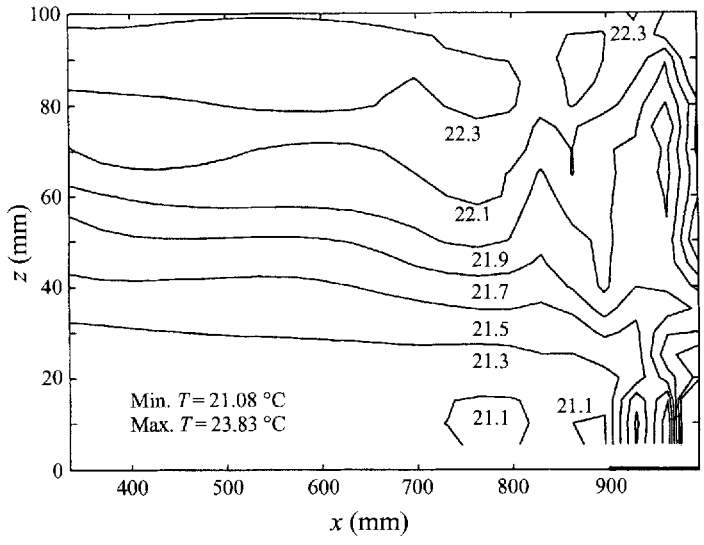

FIGURE 10. Temperature contours at $Ra = 3.32 \times 10^8$, $t/t_f > 10^2$ and $0.335 < X < 0.995$.

A temperature contour map of the tank from $X = 0.335$ to 1.0 is shown in figure 10. The time is very large compared with t_f and the experimental fluid is water. Cooling near the top wall is due to evaporation through the thermistor access ports. Contours at $X > 0.95$, where there are quickly changing conditions, are unreliable as the profiles upon which they are based were not taken simultaneously. Even so there is a true impression of vigorous activity over the hot plate and a confirmation of gentle gradients in the X-direction. The temperature gradient in the Z-direction at $Z = 0.5$ is consistent with this experiment fulfilling inequality (12).

Nusselt numbers were calculated from measured temperature and velocity profiles at the centre of the tank by integrating their product and confirming that conduction heat fluxes in either direction were not significant. The outcome is shown in figure 11(*a*), where $N^* = (h_e^{3n+1} H^{1-3n}/hL^*_{cond})\, Nu^*\, Ra^{*-n}$ is plotted against time scaled with t_f. This enables a direct comparison of the data with the constant c, which is plotted as the solid line. The value of n is 1/3 in this figure. The present results mainly lie just below this, with the most scattered points (at larger times) about 25% below c. The bulk of the points in the figure are beyond the starting transient region. The far left and upper point at $Ra = 1.15 \times 10^8$ is clearly in the transient region at $t/t_f \approx 1$. The velocity points in figure 9(*b*), with greater scatter than the rest as discussed earlier, translate to the uppermost two points of data for $Ra = 2.07 \times 10^7$. Note that the scatter in the Nusselt number results is essentially the same as that in the velocity plots. On the whole these results provide further support for the scaling of the previous section and also show that, though the tank is a long box, the interior counterflows do not substantially insulate the end regions from each other.

Our motivation is application to geophysical flows. Even so we note that values of n in equation (10) with some theoretical justification have been suggested ranging from 2/7 (Castaing *et al.* 1989) to the classical 1/3, possibly valid at 'high' Rayleigh numbers. The best empirical value is 0.293, which is distinct from, though close to, Castaing's value (Siggia 1994). To test this dependence on the value of n, we have plotted N_1^*, which is identical with N^* but for the replacement of $n = 1/3$ with 0.293. Obviously the constant c changes too, to 0.130 (Siggia 1994). The result is to be seen in figure 11(*b*), with no obvious improvement to collapsing the data onto a line and

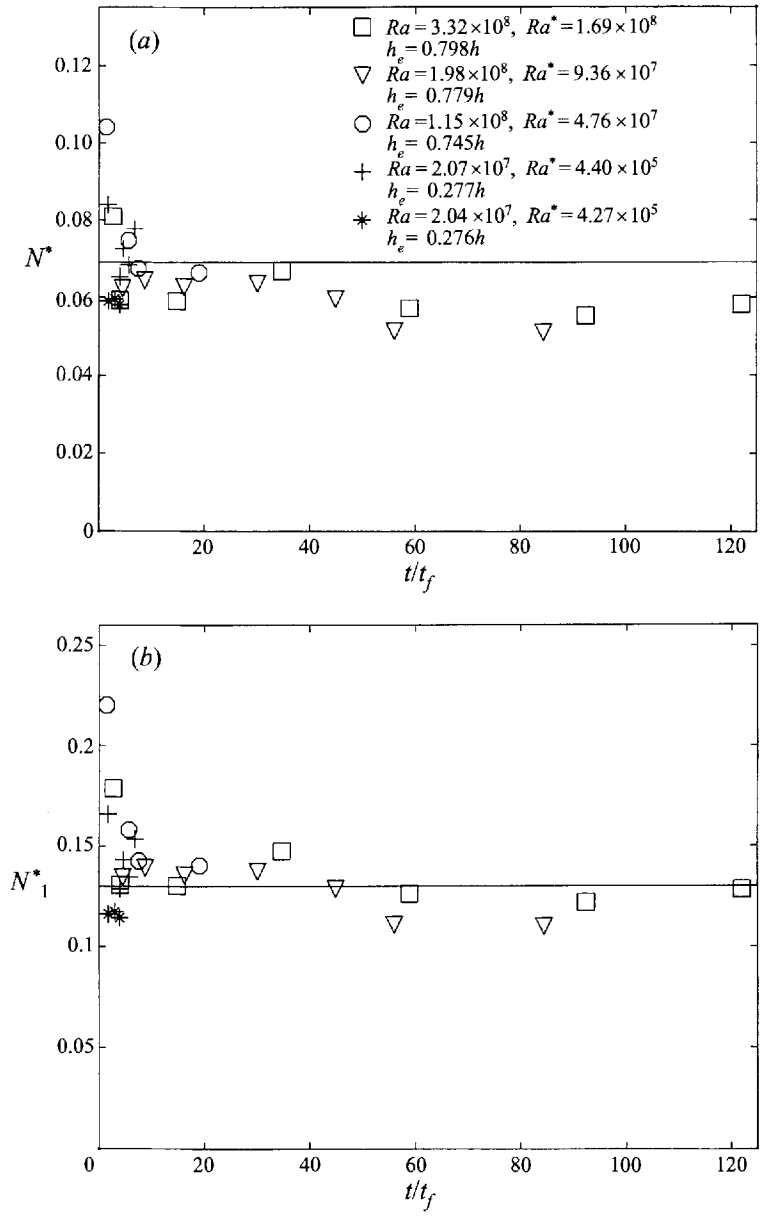

FIGURE 11. (*a*) $N^* = (h_e^{3n+1} H^{1-3n}/hL^*_{cond})\, Nu^* Ra^{*-n}$ plotted against t/t_f, compared with c in $Nu = cRa^n$, $n = 1/3$. (*b*) As (*a*) but N_1^* results from using $n = 0.293$.

perhaps even the reverse. Not too much importance should be attached to the better agreement of the data with the constant, as no reconciliation has been made in Siggia, or elsewhere to our knowledge, between the (rightly) different constants derived from data from different sources. Conversely not too much importance should be attached to the difference between our data and the constant associated with $n = 1/3$ in figure 11(*a*).

6. Concluding summary and remarks

The dynamics in long boxes with horizontally applied heating and cooling, in the unstable configuration, have flow fields in the end regions which are complex and unsteady, bearing little resemblance to what is seen in the well-studied case of boxes with heated/cooled (vertical) endwalls. At the hot plate, upon start-up there is a delay until the heated fluid becomes unstable, after which plumes of heated fluid rise rapidly. A similar sequence of events occurs at the cooled plate. Local recirculation is initially set up in the end regions which becomes less strong as intrusion layers move from the end regions into the interior of the tank, finally to encounter the opposite ends and form a tank-scale circulation. The plates which initially were occupied fully with 'turbulent' convection are now occupied near the leading edge by a laminar boundary layer, which becomes 'turbulent' in this tank about $0.2h$ from the leading edge. With the glycerol/water working fluid the situation is complicated by the presence of a viscous region near the endwall of the tank, which further reduces the size of the turbulent region.

A steady state seems not to be reached in a strict sense even at very long times, when velocity fluctuations in the interior flow are about $\pm 15\%$ of the mean values, reflecting the presence of tank-scale internal waves. The basic scaling arguments which assumed that turbulent convection occupied the entire plate were modified to reflect the actual portion of the plate occupied by turbulent convection. The classical Rayleigh–Bénard result $Nu^* \sim Ra^{*1/3}$ is sound for application to the tank. The arguments suggested that the plates would be approximately 60% occupied by laminar boundary layers at $Ra^* = 4.5 \times 10^4$, above which turbulent convection would move over an increasing proportion of the plate until at $Ra \approx 10^{14}$, 99% of the plates would be occupied by turbulent convection. Scaling arguments predicted that a non-zero vertical temperature profile would exist at the horizontal centreline of the tank, consistent with observations. These arguments also predicted that a quiescent velocity profile would exist at the horizontal centreline of the tank. At times less than or equal to the approximate filling time this was the case, but at longer times a cubic velocity profile occupied the interior of the tank. This appears to be a consequence of a separated region on the upper wall in the domain $0.8 \leqslant X \leqslant 0.9$ (and at the corresponding location at the cold plate end).

For a geophysical setting, which provided the original motivation for the study, a calculation of a lowest plausible Rayleigh number for the sidearm of a reservoir showed $Ra = 10^{11}$ for differential heating (or cooling) of 1 °C applied over a length scale of 100 m and using typical geophysical turbulent diffusivities of $O(10^{-4})$ m^2 s^{-1}. We will content ourselves with looking at the typical velocity, circulation time and volume flux for the same minimal conditions in a sidearm. Assume a typical diurnal thermocline depth of say 5 m. So $\Delta T = 1$ °C, $h = h_e = 100$ m, $L = 1000$ m, $H = 5$ m. From (7) $u \sim 0.04$ m s^{-1}, the filling time follows from (8), with $\delta = H$, as $t_f \sim 2 \times 10^4$ s and the volume flux $F_v \sim u\delta \sim uH \sim 4 \times 10^{-1}$ m^2 s^{-1} (per unit width). The corresponding buoyancy flux from the 100 m forcing zone is $\sim 10^{-8}$ m^2 s^{-3}. The velocity is substantial in geophysical terms and illustrates the importance of the mechanism explored here. The filling time is of the order of magnitude of the time scale of diurnal forcing, allowing the flows investigated here to be established on a diurnal basis.

The authors thank S. Armfield, M. Coates and the anonymous reviewers who made useful comments on an earlier version of this paper and also J. Bagrie who constructed the experimental tank. The project was supported financially by the Australian Research Council. Centre for Water Research Reference ED-772-JJS.

Appendix

The Nusselt number was evaluated essentially as the integral of uT at the vertical centreline of the tank, adjusted to an estimate of the total heat flow from plate to plate normalized by the plate-to-plate conduction heat transfer in stationary fluid. Hence

$$Nu = \frac{q_{conv_{X=0.5}} + q_{cond_{p=\infty}} - q_{conv_{Z=0.5}} - q_{cond_{Z=0.5}}}{q_{cond_{p=\infty}}}; \tag{A 1}$$

$q_{conv_{X=0.5}}$ is the horizontal convection heat flow measured across the tank vertical centreline, i.e.

$$q_{conv_{X=0.5}} = \int_0^H \rho C_p u(T-\bar{T})\,\mathrm{d}z$$

and $\bar{T}$ is the mean tank temperature; $q_{cond_{p=\infty}}$ is the conduction heat flow from plate to plate with no fluid motion, i.e.

$$q_{cond_{p=\infty}} = -\frac{kH(2\Delta T)}{\pi[(L-h_e-h_l)^2 + H^2/8]^{1/2}},$$

where $2\Delta T$ is the plate-to-plate temperature difference and the conduction path length has been approximated by assuming that the heat path is parallel to the horizontal walls of the (long) box at the centre and follows quadrants of ellipses to the ends over the plates. This amounts to about 0.4% of the (streamwise) convective flow at $Ra = 2 \times 10^8$ (0.6% for the glycerol/water mix).

The quantity $q_{conv_{X=0.5}}$ is the overestimate by $q_{conv_{Z=0.5}}$ of plate-to-plate convection due to convection across the tank horizontal centreline, i.e.

$$q_{conv_{Z=05}} \approx \int_h^{L-2h} \rho C_p w(T-\bar{T})\,\mathrm{d}x \approx 0 \quad \text{if } w = 0 \text{ at } Z = 0.5, \text{ or if } T \approx \bar{T}, \text{ or both.}$$

This is close to zero.

The quantity $q_{cond_{p=\infty}}$ is the overestimate by $q_{cond_{Z=0.5}}$ of the plate-to-plate conduction due to conduction across the horizontal centreline of the tank if a non-zero vertical velocity profile resides there, i.e.

$$q_{cond_{Z=0.5}} \approx \int_h^{L-h} k\,\partial T/\partial z|_{z=H/2}\,\mathrm{d}x.$$

This is about 4% of the convective heat flow at $Ra = 2 \times 10^8$ (5% for the glycerol/water mix).

REFERENCES

Adrian, R. J., Ferreira, R. T. D. S. & Boberg, T. 1986 Turbulent thermal convection in wide horizontal fluid layers. *Exps Fluids* **4**, 121–141.

Armfield, S. & Patterson, J. C. 1991 Direct simulation of wave interactions in unsteady natural convection in a cavity. *Intl J. Heat Mass Transfer* **34**, 929–940.

Badgley, F. J. 1966 Heat budget at the surface of the Arctic Ocean. In *Proc. Symp. on Arctic Heat Budget* (ed. J. O. Fletcher), pp. 267–277. Rand Corp.

Bejan, A. 1984 *Convection Heat Transfer*. Wiley.

Castaing, B., Gunaratne, G., Heslot, F., Kadanoff, L., Libchaber, A., Thomae, S., Wu, X.-Z., Zaleski, S. & Zanetti, G. 1989 Scaling of hard thermal turbulence in Rayleigh–Bénard convection. *J. Fluid Mech.* **204**, 1–30.

CHOU, S.-H., ATLAS, D. & YEH, E.-N. 1986 Turbulence in a convective Marine Atmospheric Layer. *J. Atmos. Sci.* **43**, 547–564.

COATES, M. C. & PATTERSON, J. C. 1993 Unsteady natural convection in a cavity with a non-uniform absorption of radiation. *J. Fluid Mech.* **256**, 133–161.

CORMACK, D. E., LEAL, L. G. & IMBERGER, J. 1974 Natural convection in a shallow cavity with differentially heated end walls. *J. Fluid Mech.* **65**, 209–229.

IMBERGER, J. & PATTERSON, J. C. 1990 Physical limnology. *Adv. Appl. Mech.* **27**, 303–475.

IVEY, G. N. 1984 Experiments on transient, natural convection in a cavity. *J. Fluid Mech.* **144**, 389–401.

IVEY, G. N. & HAMBLIN, P. F. 1989 Convection near the temperature of maximum density for high Rayleigh number, low aspect ratio rectangular cavities. *Trans. ASME* C: *J. Heat Transfer* **111**, 100–105.

KILLWORTH, P. D. 1983 Deep convection in the world ocean. *Rev. Geophys. Space Phys.* **21**, 1–26.

LEMKERT, C. & IMBERGER, J. 1993 Energetic bubble plumes in arbitrary stratification. *J. Hydraul. Engng ASCE* **119**, 680–703.

LINDEN, P. F. & SIMPSON, J. 1986 Gravity-driven flows in a turbulent fluid. *J. Fluid Mech.* **172**, 481–497.

MALANOTTE-RIZZOLI, P. 1991 The Northern Adriatic Sea as a prototype of convection and water mass formation on the continental shelf. In *Deep Convection and Deep Water Formation in the Oceans* (ed. P. C. Chu & J. C. Gascard), pp. 229–239. Elsevier.

MAXWORTHY, T. & MONISMITH, S. G. 1988 Differential mixing in a stratified fluid. *J. Fluid Mech.* **189**, 571–598.

MITSUMOTO, S., UEDA, H. & OZOE, H. 1983 A laboratory experiment on the dynamics of the land and sea breeze. *J. Atmos. Sci.* **40**, 1228–1240.

MONISMITH, S., IMBERGER, J. & MORISON, M. L. 1990 Convective motions in the sidearm of a small reservoir. *Limnol. Oceanogr.* **35**, 1676–1702.

MORISON, J. H., MCPHEE, M. G., CURTIN, T. B. & PAULSON, C. A. 1992 The oceanography of winter leads. *J. Geophys. Res.* **97**, 11199–11218.

NOH, Y., FERNANDO, H. J. S. & CHING, C. Y. 1992 Flows induced by the impingement of a two-dimensional thermal on a density interface. *J. Phys. Oceanogr.* **22**, 1207–1219.

PATTERSON, J. C. & ARMFIELD, S. W. 1990 Transient features of natural convection in a cavity. *J. Fluid Mech.* **219**, 469–497.

PATTERSON, J. C. & IMBERGER, J. 1980 Unsteady natural convection in a rectangular cavity. *J. Fluid Mech.* **100**, 65–86.

PHILLIPS, O. M. 1966 On turbulent convection currents and the circulation of the Red Sea. *Deep-Sea Res.* **13**, 1149–1160.

ROSSBY, H. T. 1969 A study of Bénard convection with and without rotation. *J. Fluid Mech.* **36**, 309–335.

SCHLICHTING, H. 1968 *Boundary-Layer Theory*. McGraw-Hill.

SIGGIA, E. D. 1994 High Rayleigh number convection. *Ann. Rev. Fluid Mech.* **26**, 137–168.

STEVENS, C. S. & COATES, M. J. 1994 A maximised cross-correlation technique for resolving velocity fields in laboratory experiments. *J. Hydraul. Res.* **32**, 195–211.

STURMAN, J. J., IVEY, G. N. & TAYLOR, J. R. 1992 Convection in a long rectangular box driven by heated and cooled segments of the horizontal boundaries. *Proc. 11th Australasian Fluid Mechanics Conference*, vol. II, pp. 1005–1008.

TURNER, J. S. 1973 *Buoyancy Effects in Fluids*. Cambridge University Press.

WILLERT, C. E. & GHARIB, M. 1991 Digital particle image velocimetry. *Exps. Fluids* **10**, 181–193.